JOURNAL OF CATALYSIS **176,** 426–438 (1998)
ARTICLE NO. CA982069

Iron-Oxide Supported Gold Catalysts Derived from Gold-Phosphine Complex $Au(PPh_3)(NO_3)$: State and Structure of the Support

Anguelina P. Kozlova,* Sho Sugiyama,* Alexander I. Kozlov,* Kiyotaka Asakura,† and Yasuhiro Iwasawa*,[1]

*Department of Chemistry; and †Research Center for Spectrochemistry, Graduate School of Science, The University of Tokyo, Hongo, Bunkyo-ku, Tokyo 113-0033, Japan

Received November 21, 1997; revised March 3, 1998; accepted March 4, 1998

Iron oxide supported gold catalysts were prepared by supporting the Au-phosphine complex $Au(PPh_3)(NO_3)$ onto various iron oxide supports. Among the prepared catalysts only the use of amorphous as-precipitated iron hydroxide $Fe(OH)_3^*$ as a support for $Au(PPh_3)(NO_3)$ allowed us to obtain the tremendously active catalytic material for low-temperature CO oxidation. The supports and the Au catalysts were characterized by BET, SEM, XRD, FT-IR, XPS, and Raman. Initial structures of the employed supports were found to influence dramatically the gold particle size and the catalytic activity. The most active catalyst consisted of small gold particles and poorly crystallized iron oxide support with a mixture of α-Fe_2O_3 and γ-Fe_2O_3. The γ-Fe_2O_3 formation occurred by the presence of the PPh_3 as a ligand for gold. The presence of γ-Fe_2O_3 influenced positively the catalytic activity of the Au-containing samples.

INTRODUCTION

Metal particles supported on metal oxides are of lasting interest because of their wide applications to a variety of catalytic reactions (1, 2). While many researchers have been concerned with Pt group metals, catalysis of Au has been little studied because Au was traditionally regarded as a poorly active component in catalytic systems. Ozin and co-workers found high reactivity of Au atoms condensed with CO/O_2 mixtures at 10 K for the oxidation of CO to CO_2 (3). However, for a long time the interest towards supported gold catalysts was to a large extent theoretical, until Haruta and co-workers reported a possibility for dramatic improvement of their catalytic activity using a coprecipitation method (4). The catalytic materials, prepared by coprecipitation of $HAuCl_4$ and a metal nitrate, exhibited high catalytic activity in low-temperature CO oxidation (4–6). Works on supported gold catalysts done so far reveal that the dramatic changes in the catalytic activity occur only when gold is in a highly dispersed state. It has also been reported that Au/M_xO_y catalysts (M_xO_y = metal oxide where M = Fe, Co, Ti, etc.) are active in a number of important reactions including complete oxidation of hydrocarbons (7), hydrogenation (8), water gas shift reaction (9, 10), and NO reduction (11). The supported gold catalysts were found to be able to compete with commercially applied catalysts in operating temperatures, activities, and life times (9, 10, 12–14). These findings have given new impulse to intensive studies on both the origin of the unique high activity and the search for novel preparation techniques of finely dispersed gold on metal oxides (15, 16).

Recently we have showed that Au-PPh_3 complexes provide a new way to obtain supported Au catalysts on a variety of metal oxides (17, 18). The feature of the preparation procedure involves supporting the gold complexes from organic media onto as-precipitated metal hydroxides. The Au catalysts derived from a Au-PPh_3 complex and Mn, Co, Ni, and Fe as-precipitated hydroxides showed remarkably high activities for CO oxidation even at as low temperatures as 200 K. In contrast, conventional oxide-derived Au catalysts exhibited much poorer catalytic performances. The most pronounced difference was observed for Au/Fe oxide systems. Estimation of Au particles size by TEM gave mean gold particle sizes of 2.9 for the $Au/Fe(OH)_3^*$ and 30 nm for Au/Fe_2O_3 samples (18). These results suggested that the initial state and nature of the support strongly influence on both Au particle size and CO oxidation activity. To understand the origin of the support effect on the catalytic activity of supported gold catalysts, detailed comparison of various types of supports is necessary. To produce and stabilize small metal particles, interactions between metal precursor and supporting material during the course of preparation seem to be important. Concentration of hydroxyl groups may also be regarded as an important feature of metal oxide surface to obtain small metal particles (19).

The present paper is reported as a part of the detailed study on the Au/Fe oxide catalysts, prepared by supporting the phosphine-ligated Au complex $Au(PPh_3)(NO_3)$ to specially prepared and commercially available supports. We will show that careful selection of supports is a key issue

[1] To whom all correspondence should be addressed. E-mail: iwasawa@chem.s.u-tokyo.ac.jp.

0021-9517/98 $25.00

in creating highly active Au catalysts. To elucidate the effect of initial states and structures of iron-oxide supports, characterization of the supports and final catalysts has been performed. In this paper we report chemico-physical characteristics of the supports investigated by BET, SEM, XRD, FT-IR, XPS, and Raman. Detailed characterization of Au-species of the Au/Fe oxide catalysts by means of TEM, XPS, and EXAFS will be reported in a separate paper.

EXPERIMENTAL

Sample Preparation

$Fe(NO_3)_3 * 9H_2O$ and Na_2CO_3 (both from Wako Chemical Co., 99.9%) were used as the starting materials for preparation of the $Fe(OH)_3^*$. $Au(PPh_3)(NO_3)$ was synthesized according to the literature (20) (calculated for $C_{18}H_{15}AuNO_3P$: C, 41.48; H, 2.90; N, 2.69. Found: C, 41.60; H, 3.01; N, 2.68).

The $Au/Fe(OH)_3^*$ sample was obtained by supporting the gold complex $Au(PPh_3)(NO_3)$ on as-precipitated wet iron hydroxide $Fe(OH)_3^*$, in a similar manner to the literature (17, 18). In a typical procedure, an aqueous solution of $Fe(NO_3)_3 * 9H_2O$ (20.79 mmol in 400 ml H_2O) was added dropwise (8 ml/min) to an aqueous solution of Na_2CO_3 (69.81 mmol in 200 ml H_2O) under vigorous stirring. Final pH of the mixture was ca 9.1. After 3 h of aging at room temperature (RT), the brown precipitate was filtered and washed several times with distilled water until the percolated water showed pH 7. The resultant iron hydroxide $Fe(OH)_3^*$ was immediately used for impregnation with the gold complex. The $Fe(OH)_3^*$ was thoroughly pounded in 100 ml of acetone to obtain a fine suspension, and then an acetone solution of the $Au(PPh_3)(NO_3)$ was added under stirring. The acetone was slowly removed by vacuum evaporation for 4 h at RT, and the obtained sample was treated by temperature-programmed calcination in a flow of air (30 ml/min) prior to using as a catalyst. The general procedure for the calcination was as follows: the sample was heated up to 673 K at a heating rate of 4 K/min; then the temperature was kept for 4 h. The catalyst thus obtained is denoted as $Au/Fe(OH)_3^*$. The preparation procedure allowed us to obtain good reproducibility in all independent preparations of the $Au/Fe(OH)_3^*$ catalysts.

We also prepared Au catalysts by using iron oxide supports $Fe(OH)_3^*$-dried and $Fe_2O_3^*$, which were obtained by vacuum drying of $Fe(OH)_3^*$ at RT for 1.5 h and by calcination of $Fe(OH)_3^*$-dried at 773 K, respectively. These samples, denoted as $Au/Fe(OH)_3^*$-dried and $Au/Fe_2O_3^*$, respectively, were prepared by impregnating the supports with $Au(PPh_3)(NO_3)$, followed by the similar solvent evaporation and calcination procedures to those for $Au/Fe(OH)_3^*$.

Au/Fe_2O_3-coprecipitated sample was obtained according to the literature (5, 6). An aqueous mixture of $Fe(NO_3)_3 * 9H_2O$ and $HAuCl_4$ (Au : Fe ratio = 1/19) was added to an aqueous solution of Na_2CO_3 (final pH = 9.1), followed by washing with hot water until no Cl^- was detected, drying in vacuum, and calcination in the same manner as for the $Au/Fe(OH)_3^*$ sample. Au loading in the Au/Fe_2O_3-coprecipitated sample was determined by XRF to be 4.1 wt%.

Samples symbolized by CA were prepared by impregnating $Au(PPh_3)(NO_3)$ on commercially available (CA) supporting materials, followed by the same solvent evaporation and calcination procedures as those for $Au/Fe(OH)_3^*$. Among the CA materials used as supports or as reference samples, α-Fe_2O_3 CA was obtained from Wako Chemical Co. and all the other CA materials (γ-Fe_2O_3 CA, α-FeOOH CA, γ-FeOOH CA, $Fe(OH)_3$ CA, Fe_3O_4 CA) were purchased from Soekawa Chemical Co.

To elucidate the effect of the remaining P species in the catalysts, a $Fe(OH)_3^*${P} sample was prepared by impregnation of $Fe(OH)_3^*$ with an acetone solution of PPh_3, instead of $Au(PPh_3)(NO_3)$. The material was treated by the temperature-programmed calcination before use as a catalyst, similarly to other catalysts.

For all supported Au catalysts, except for coprecipitated Au/Fe_2O_3, Au loading was 3 wt% (analyzed by XRF).

Sample Characterization

SEM images of powder samples mounted on copper holders were obtained on a JEOL SM-6340F instrument, operated at 15 kV, or on a JEOL JSM-6320F instrument, operated at 10 kV (for Pt-sputtered samples).

The surface areas of the samples were measured by a conventional BET nitrogen adsorption method (N_2 99.9999%, Takachiho Chemical Co.) at 77 K using a BELSORP36 machine. Before the measurements, samples of about 0.3 g were pretreated at 573 K for 3 h in a vacuum using a turbo molecular pump.

XRD patterns were recorded on a Rigaku X-ray diffractometer operated at 35 kV and 15 mA using nickel-filtered Cu-K_α radiation and at a scanning speed $2^\circ(2\theta)$/min using a $1/2^\circ$ divergence slit and a 0.15 mm receiving slit. Powder samples were mounted on glass holders with a small amount of grease (Apiezon H).

X-ray photoelectron spectra were recorded by using a Rigaku XPS 7000 spectrometer with Mg Kα radiation as the X-ray excitation source. The measurements were performed under pressures less than 5×10^{-7} Pa. The electron binding energies were referenced to C 1s (BE = 284.6 eV) peak (21).

Raman spectra were recorded with a Renishaw Raman Microscope at the ambient conditions; a He-Ne laser at 632 nm was used as an excitation source. The laser power was 30 mW. The spectra were taken with a resolution of 4 cm^{-1}; three scans for each sample were averaged.

FT-IR spectra were measured in a transmission mode on a JASCO FTIR 230 spectrometer at a spectral resolution of 4 cm^{-1}. The measurements were conducted in an *in situ* IR cell combined in a closed circulating system. Sample powders were pressed into self-supported thin disks with a diameter of 2 cm. The sample disks were heated (4 K/min) under 13.3 kPa of O_2 from 298 to 673 K.

Catalytic Performance

The catalytic performance of the samples for CO oxidation was carried out in a glass fixed-bed flow reactor equipped with a computer-controlled auto-sampling system at atmospheric pressure. A reaction gas mixture (1.0% CO balanced with air, Takachiho Chemical Co.) was passed through the catalyst bed (200 mg of catalyst) at a flow rate of 67 ml/min (SV = 20,000 ml/h/g). The effluent gas was analyzed by a gas chromatograph using a Unibeads C column (GL Sciences) for CO_2 and a 5 Å molecular sieve column (GL Sciences) for CO and O_2. The catalytic activity was expressed as degree of CO conversion.

RESULTS

Catalytic CO Oxidation

We compared the catalytic performance of several Au-containing samples derived from various supports. Catalytic activities (expressed as degree of CO conversion) of Au/Fe(OH)$_3^*$, Au/Fe(OH)$_3^*$-dried, Au/$Fe_2O_3^*$, Au/Fe(OH)$_3$ CA, Au/α-FeOOH CA, and Au/α-Fe_2O_3 CA are plotted as a function of the reaction temperature in Fig. 1. The data show clearly that only the application of as-precipitated wet iron hydroxide Fe(OH)$_3^*$ allowed us to obtain the Au catalyst with extremely high activity toward CO oxidation at as low temperatures as 200 K. The steady-state reaction rates for several Fe-oxide supported Au catalysts active for low-temperature CO oxidation are summarized in Table 1. The Au/Fe(OH)$_3^*$ catalyst showed a higher activity than the Au/Fe_2O_3-coprecipitated sample for CO oxidation at low temperatures (Fig. 1). Amounts of adsorbed water and surface hydroxyls of the support on which the gold precursor was impregnated seem to be very important because the decrease in the water and hydroxyl contents of the Fe(OH)$_3^*$ by drying and calcination resulted in lowering the catalytic activity of the Au catalysts in the order for support: Au/Fe(OH)$_3^*$ > Au/Fe(OH)$_3^*$-dried ≫ Au/$Fe_2O_3^*$ (Fig. 1). It should be noted that the decrease of the catalytic performance caused by the RT-drying of the as-precipitated Fe(OH)$_3^*$ support was not so drastic as that caused by the further heat treatment of the support, and the Au/Fe(OH)$_3^*$-dried sample showed ~20% of CO conversion even at 200 K. On the other hand, the use of commercially available supports including wet Fe(OH)$_3$ CA produced the catalysts which are active for CO oxidation only at elevated temperatures.

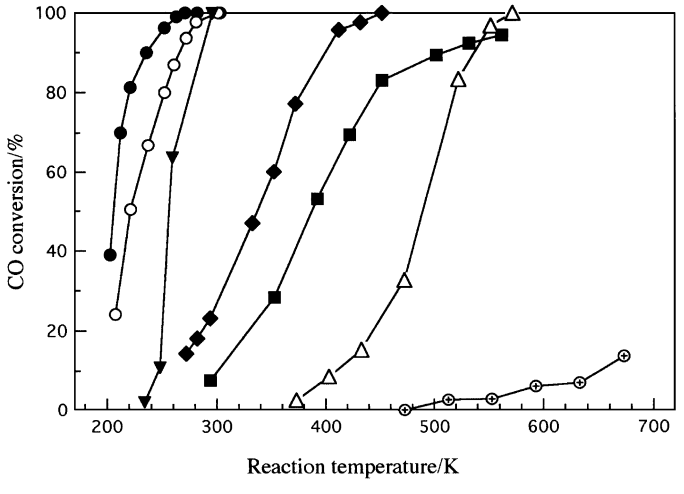

FIG. 1. Catalytic performance of various Au(PPh_3)(NO_3)-derived iron oxide supported catalysts and a coprecipitated Au/Fe_2O_3 catalyst, calcined at 673 K for 4 h: (—●—) Au/Fe(OH)$_3^*$; (—○—) Au/Fe(OH)$_3^*$-dried; (—▼—) Au/Fe_2O_3-coprecipitated; (—◆—) Au/α-FeOOH CA; (—■—) Au/$Fe_2O_3^*$; (—△—) Au/Fe(OH)$_3$ CA; (—⊕—) Au/α-Fe_2O_3 CA.

TABLE 1

Reaction Rates for Low-Temperature CO Oxidation on Iron Oxide Supported Au Catalysts

Catalyst	Au (wt%)	CO conv. (%)	T (K)	Rate [mol CO (mol-Au)$^{-1}$ s^{-1}]	Ref.
Au/Fe(OH)$_3^*$ (0.2 g)	3	39	203	0.0064	This work
Au/Fe(OH)$_3^*$-dried (0.2 g)	3	24	208	0.0039	This work
Au/Fe_2O_3-copr (0.2 g)	4.1	2	234	0.0002	This work
Au/Fe_2O_3 (0.2 g)	11.5	60	203	0.0026	(6)
Au/Fe_2O_3 (0.05 g)	0.66	<10	304	<0.0298	(6)
Au/Fe_2O_3 (0.15 g)	0.56	4	251	0.0342	(43)

Figure 2 shows a comparison between catalytic activities of various samples containing α-Fe_2O_3 and γ-Fe_2O_3 in CO oxidation. Without the supporting Au, the iron oxide supports were active for CO oxidation only at temperatures higher than 400 K. Among them, the $Fe_2O_3^*$ support prepared from Fe(OH)$_3^*$ was the most active one, and the order of the activities for a series of the supports was as follows: $Fe_2O_3^*$ > α-Fe_2O_3 CA ≈ Fe(OH)$_3^*${P} ≫ γ-Fe_2O_3 CA. Pure α-Fe_2O_3 CA support is much more active for CO oxidation than pure γ-Fe_2O_3 CA. However, by impregnating those iron oxides with Au(PPh_3)(NO_3), the order of the catalytic activities changed as follows: Au/FeOH$_3^*${P} > Au/$Fe_2O_3^*$ > Au/γ-Fe_2O_3 CA > Au/α-Fe_2O_3

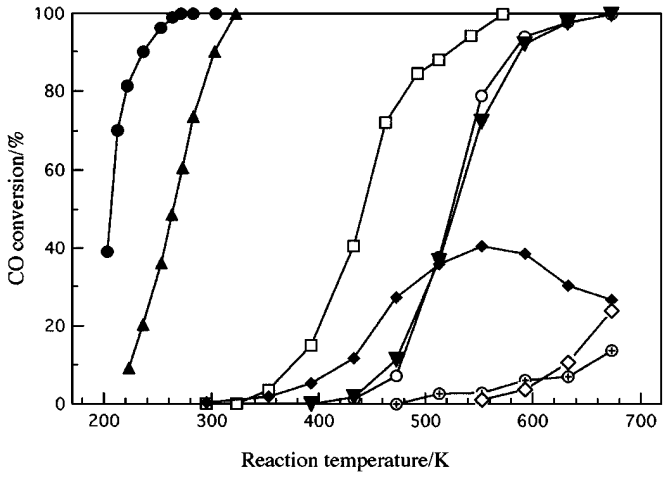

FIG. 2. Catalytic performance of various iron oxide supports and Au-containing samples: (—●—) Au/Fe(OH)$_3^*$; (—▲—) Au/Fe(OH)$_3^*${P}; (—□—) $Fe_2O_3^*$; (—○—) α-Fe_2O_3 CA; (—▼—) Fe(OH)$_3^*${P}; (—◆—) Au/γ-Fe_2O_3 CA; (—⊕—) Au/α-Fe_2O_3 CA; (—◇—) γ-Fe_2O_3 CA.

CA as shown in Fig. 2 (see also Fig. 1). It is to be noted that the Au/Fe(OH)$_3^*${P} sample showed a much higher activity than the Au/$Fe_2O_3^*$ sample, with 90% CO conversion at room temperature.

SEM Measurements

SEM images of α-Fe_2O_3 CA, $Fe_2O_3^*$, Fe(OH)$_3^*${P}, and gold-containing sample Au/Fe(OH)$_3^*$ after calcination at 673 K are shown in Fig. 3. The SEM images clearly showed a decrease in the particle size of the iron oxides in the series of α-Fe_2O_3 CA (ca 150 nm) > specially prepared $Fe_2O_3^*$ (ca 45 nm) > Fe(OH)$_3^*${P} $\approx$ Au/Fe(OH)$_3^*$ (ca 15 nm). For the Fe(OH)$_3^*${P} and Au/Fe(OH)$_3^*$ samples the average size of the primary units is about 3 and 10 times smaller than those of the $Fe_2O_3^*$ and commercially available α-Fe_2O_3 CA, respectively. Moreover, the shape of the primary crystals of the Fe(OH)$_3^*${P} and Au/Fe(OH)$_3^*$ samples becomes very irregular and defective, and their arrangement is highly disordered (Figs. 3c and 3d), in contrast to the images of α-Fe_2O_3 CA and $Fe_2O_3^*$ (Figs. 3a and 3b).

BET Measurements

The BET surface areas (S_{BET}) for iron-oxide supported Au catalysts are summarized in Table 2. The S_{BET} decreases for the series of Au/α-FeOOH CA > Au/$Fe_2O_3^*$ > Au/Fe(OH)$_3$ CA > Au/α-Fe_2O_3 CA. In agreement with the SEM data in Fig. 3, specially prepared iron oxide $Fe_2O_3^*$ possesses about 10 times larger specific surface area, as compared to α-Fe_2O_3 CA. However, the S_{BET} value for the highly active Au/Fe(OH)$_3^*$ was found to be comparable with the S_{BET} for the much less active Au/$Fe_2O_3^*$ catalyst. The S_{BET} values for Au/Fe(OH)$_3^*$-dried (57 m^2 g^{-1}) and Au/Fe(OH)$_3^*${P} (69 m^2 g^{-1}) also fall into the similar S_{BET} range.

XRD Measurements

Figure 4 represents XRD patterns of various supports used for Au(PPh_3)(NO_3): Fe(OH)$_3^*$-dried, Fe(OH)$_3$ CA-dried, α-FeOOH CA, $Fe_2O_3^*$, α-Fe_2O_3 CA, and Fe(OH)$_3^*${P}. XRD of the as-precipitated wet Fe(OH)$_3^*$ and Fe(OH)$_3$ CA were not measured in our X-ray diffractometer because it was not convenient. The Fe(OH)$_3^*$ was dried in vacuum for 1.5 h before XRD measurement. The treatment did not cause crystallization resulting in completely amorphous material (Fig. 4a). No XRD peak was observed in the Fe(OH)$_3^*$-dried sample in the 2Θ range between 20–70°. On the contrary, commercially available iron hydroxide Fe(OH)$_3$ CA after drying in a vacuum at RT revealed an XRD pattern similar to that of α-FeOOH CA (Figs. 4b and 4c, respectively); i.e. the material possesses a pronounced degree of crystallinity. $Fe_2O_3^*$ also exhibited an XRD pattern of crystalline solid corresponding to α-Fe_2O_3 (Figs. 4d and 4e, respectively). The XRD pattern of Fe(OH)$_3^*${P} (Fig. 4f) showed broad peaks of low intensity with positions mainly corresponding to α-Fe_2O_3. However, the pattern possessed the intensity ratio $I_{33.2°}/I_{35.5°} = 0.48$ which is different from that for α-Fe_2O_3 and it exhibited an additional peak at 30.2° which is not observed for α-Fe_2O_3. Analysis of selected XRD data is given in Table 2.

XRD patterns for the gold-containing samples after temperature-programmed calcination at 673 K for 4 h, Au/Fe(OH)$_3^*$, Au/Fe(OH)$_3$ CA, Au/α-FeOOH CA, Au/$Fe_2O_3^*$, Au/α-Fe_2O_3 CA, and Au/Fe(OH)$_3^*${P}, are given in Fig. 5. An XRD peak appeared at 38.2° for all the samples, except for Au/Fe(OH)$_3^*$ and Au/Fe(OH)$_3^*${P}, which corresponds to Au(111) of Au particles as a result of Au(PPh_3)(NO_3) decomposition during the calcination. The peak is well pronounced for the Au/Fe(OH)$_3$ CA sample, and the mean size of the Au crystallites formed on the Fe(OH)$_3$ CA was estimated to be about 23 nm using the Scherrer equation. Small Au(111) peaks were also observed

TABLE 2

N_2-BET Surface Areas and the 50%-Conversion Temperatures as the Scale of Catalytic CO Oxidation Activities for Various Iron Oxide-Supported Au Catalysts Calcined at 673 K for 4 h

Catalyst	$T_{50\%}$/K	Surface area/m^2 g^{-1}
Au/Fe(OH)$_3^*$	206	63[a]
Au/Fe(OH)$_3^*$-dried	223	57
Au/α-FeOOH CA	337	84
Au/$Fe_2O_3^*$	388	55
Au/Fe(OH)$_3$ CA	490	47
Au/α-Fe_2O_3 CA	—[b]	5
Au/Fe(OH)$_3^*${P}	263	60

[a] The surface areas were measured with a number of Au/Fe(OH)$_3^*$ samples and found to be in the range of 50–75 m^2 g^{-1}.

[b] The 50% conversion was not reached until 773 K.

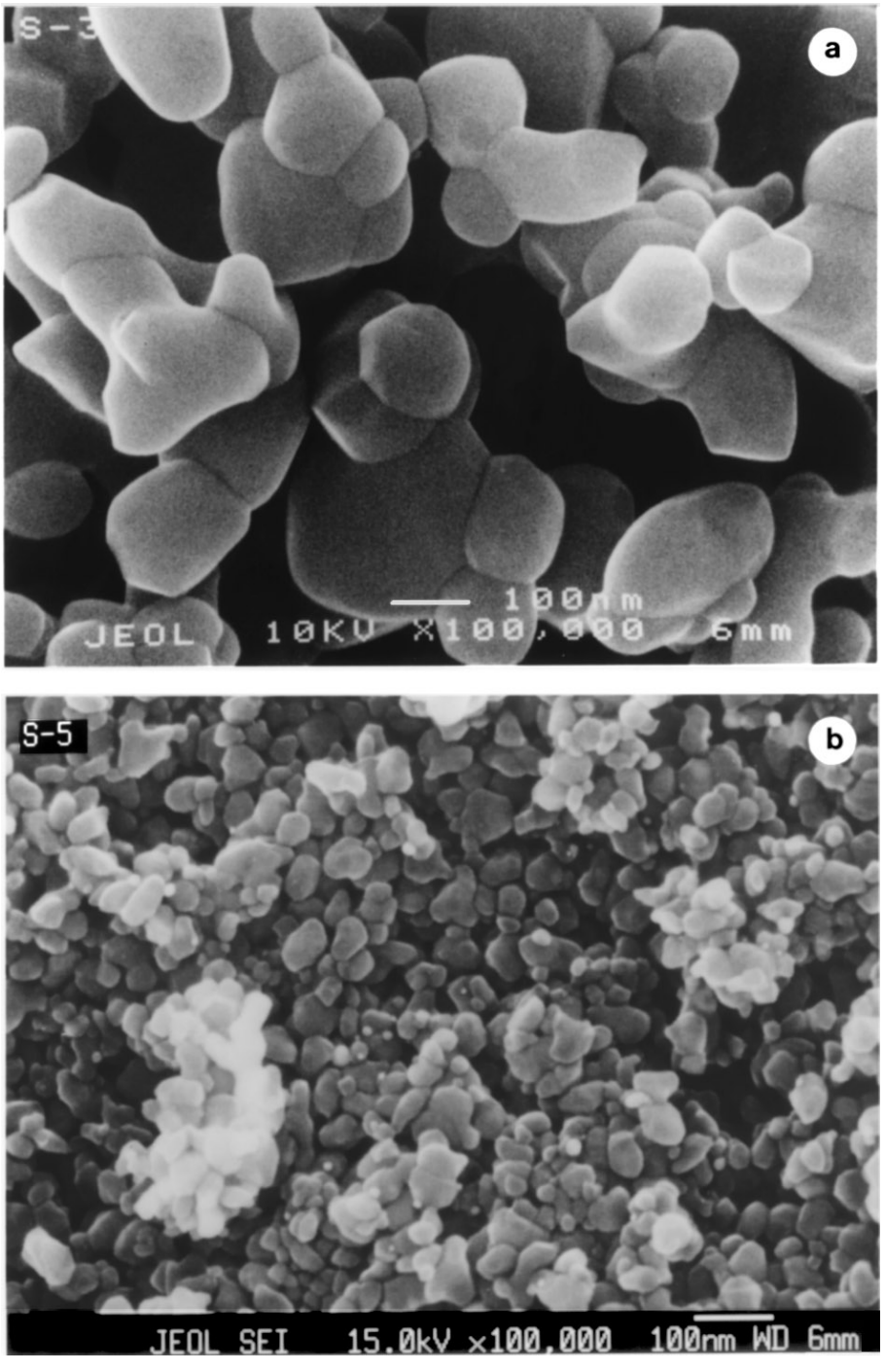

FIG. 3. SEM images of iron oxide supports: (a) α-Fe_2O_3 CA; (b) specially prepared $Fe_2O_3^*$; (c) $Fe(OH)_3^*${P}; and (d) $Au/Fe(OH)_3^*$.

for Au/α-FeOOH CA, Au/$Fe_2O_3^*$, and Au/α-Fe_2O_3 CA samples. On the other hand, the XRD peaks due to Au(111) in the case of the $Au/Fe(OH)_3^*$ and $Au/Fe(OH)_3^*${P} samples were not detected, which implies the formation of Au metal particles less than 3–4 nm.

The XRD patterns of the supported Au catalysts after calcination at 673 K for 4 h (Fig. 5) show the presence of α-Fe_2O_3 as a common feature for all the samples. The degree of support crystallinity for the Au catalysts changes as follows: $Au/Fe(OH)_3^* \approx Au/Fe(OH)_3^*${P} < $Au/Fe(OH)_3$ CA $\approx$ Au/α-FeOOH CA < $Au/Fe_2O_3^*$ < Au/α-Fe_2O_3 CA. The $Au/Fe(OH)_3^*$ and $Au/Fe(OH)_3^*${P} samples reveal the lowest intensities of the diffraction lines of α-Fe_2O_3. Besides, the XRD spectra of those samples show an additional

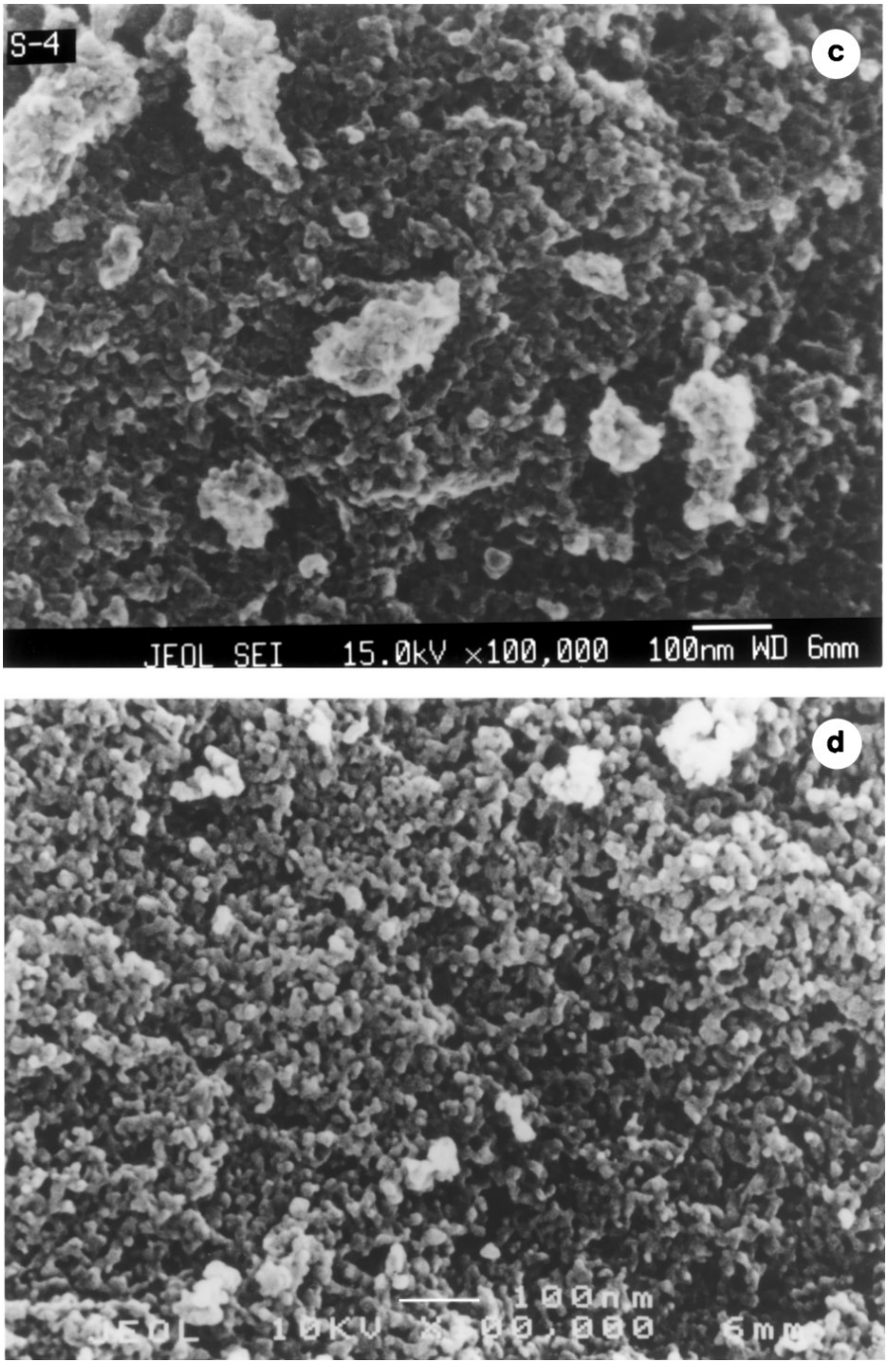

FIG. 3—*Continued*

broad line at 2Θ values of 30° (Figs. 5a and 5f), which cannot be assigned to hematite α-Fe_2O_3. The XRD data are summarized in Table 3 in the range of 2Θ values from 20° to 40°, where the most intense peaks of all the iron oxide polymorphs are presented. Table 3 indicates that the XRD peak at 30° can be ascribed to either γ-Fe_2O_3 or Fe_3O_4, or it suggests a superposition of two crystalline phases. Table 3 also shows the intensity ratio of the peak at 33.2° (the most intense hematite peak) to the peak at 35.5° (most intense peak for γ-Fe_2O_3 and for magnetite, overlapping with the 78% intensity of α-Fe_2O_3 peak). In the case of pure α-Fe_2O_3 the intensity ratio $I_{33.2^\circ}/I_{35.5^\circ}$ is assumed to be 1.27, with the ratio going to 0.0 when the α-Fe_2O_3 content is diminished. It can be seen that the ratios for Au/$Fe_2O_3^*$ and Au/$Fe(OH)_3$ CA are near 1, while for Au/$Fe(OH)_3^*$ and Au/$Fe(OH)_3^*${P} samples the ratios are about 3 times smaller (0.41–0.47)

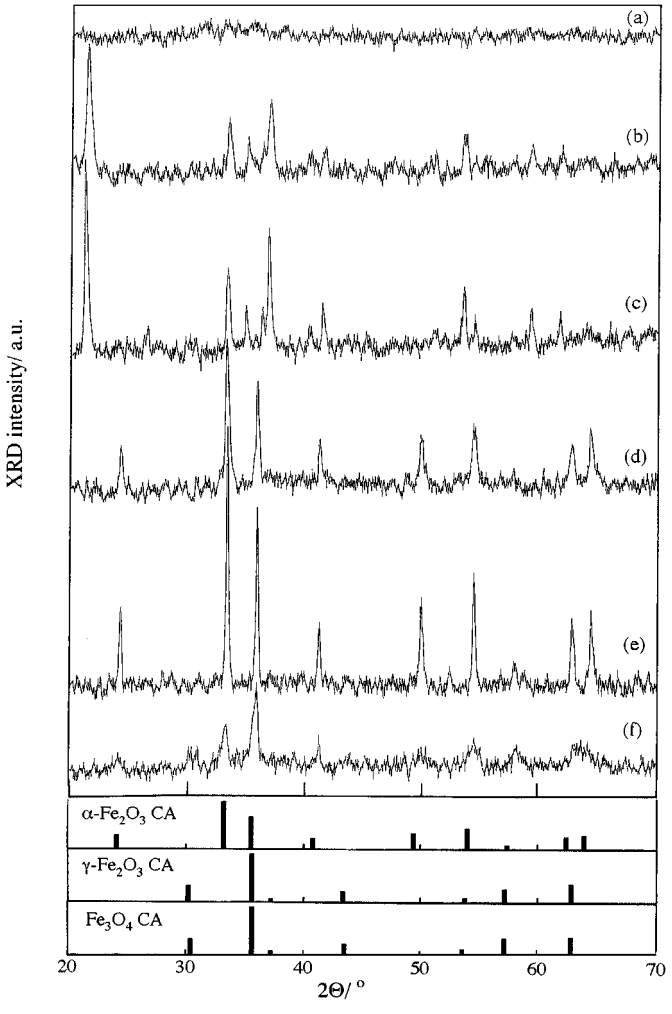

FIG. 4. XRD patterns of various supports used for $Au(PPh_3)(NO_3)$: (a) $Fe(OH)_3^*$-dried; (b) $Fe(OH)_3$ CA; (c) α-FeOOH CA; (d) $Fe_2O_3^*$; (e) α-Fe_2O_3 CA; (f) $Fe(OH)_3^*${P}.

than that for pure α-Fe_2O_3 (1.27). It should be noted that the analysis ignores X-ray amorphous phases that also may be present in the samples.

Surface Characterization by X-Ray Photoelectron and Raman Spectroscopies

XPS Fe 2p spectra of $Au/Fe(OH)_3^*$(RT) before calcination, $Au/Fe(OH)_3^*$ (473 K) after calcination at 473 K, $Au/Fe(OH)_3^*$ after calcination at 673 K, and $Fe_2O_3^*$ are given in Fig. 6. For the $Au/Fe(OH)_3^*$(RT) sample the Fe $2p_{3/2}$ XPS peak was observed at BE = 711.1 eV (Fig. 6a). Both the Fe $2p_{3/2}$ peak position and a shake-up satellite between 719–720 eV are characteristic of Fe(3+) species (22, 23). In the XPS spectrum for the $Au/Fe(OH)_3^*$ (473 K) sample the position of the Fe $2p_{3/2}$ peak is a little shifted to 710.8 eV (Fig. 6b). A broadened satellite structure can be distinguished in the spectrum 6b. The XPS spectrum of the $Au/Fe(OH)_3^*$ sample in Fig. 6c showed the Fe $2p_{3/2}$ peak at 711.3 eV. The $2p_{3/2}$ and satellite peaks for $Fe_2O_3^*$ (Fig. 6d) were observed at 711.5 and ~719.5 eV, respectively, which are close to those for $Au/Fe(OH)_3^*$.

XPS O 1s spectra obtained from the same samples as those in Fig. 6 are shown in Fig. 7. $Au/Fe(OH)_3^*$(RT) and $Fe_2O_3^*$ exhibited the O 1s peak centered at 530.1 eV (Figs. 7a and 7d). Positions of the main O 1s peak for the calcined samples $Au/Fe(OH)_3^*$ (473 K) and $Au/Fe(OH)_3^*$ (Figs. 7b and 7c) were a little shifted to lower energies by ~0.3 eV. The obtained BE values are typical ones for various M_xO_y species, and the O 1s peaks for all iron oxide polymorphs were observed in the same range. In addition, a shoulder between 531–532 eV was observed for both $Fe_2O_3^*$ and $Au/Fe(OH)_3^*$ samples. The broad shoulder of $Au/Fe(OH)_3^*$(RT) gradually decreased under the calcination as shown in Fig. 7.

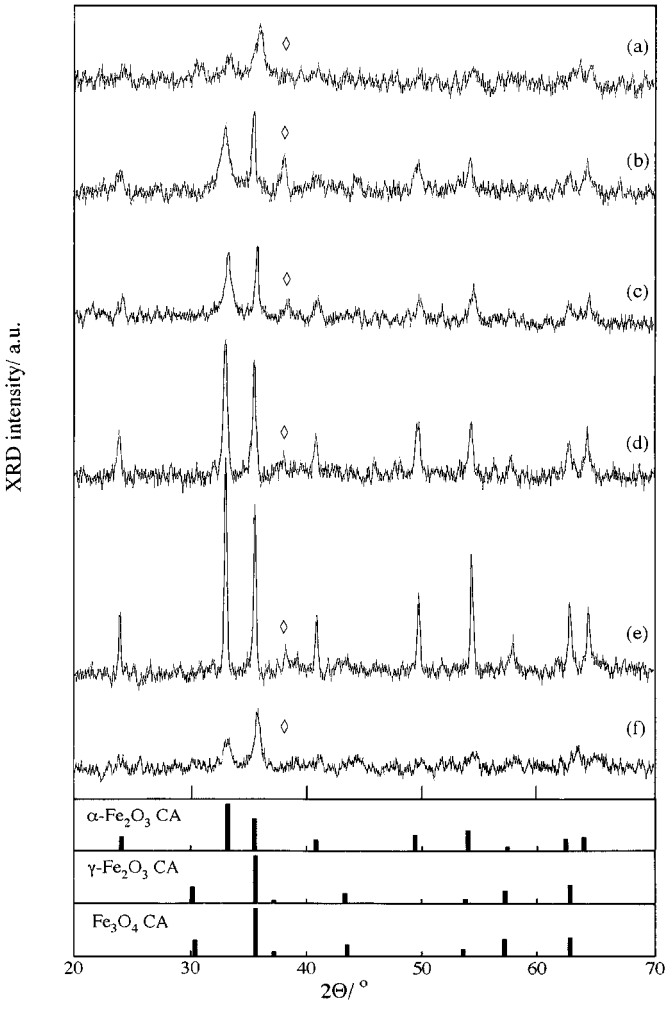

FIG. 5. XRD patterns of various $Au(PPh_3)(NO_3)$-derived iron oxide supported catalysts after calcination at 673 K for 4 h: (a) $Au/Fe(OH)_3^*$; (b) $Au/Fe(OH)_3$ CA; (c) Au/α-FeOOH CA; (d) $Au/Fe_2O_3^*$; (e) Au/α-Fe_2O_3 CA; (f) $Au/Fe(OH)_3^*${P}. ◇ indicates the position of Au(111) peak.

TABLE 3

Analysis of Selected XRD Data in the Region 20–40° 2Θ

Sample	XRD peaks positions					$I_{33.2°}/I_{35.5°}$
$Au/Fe(OH)_3^*$	24.1	30.2	33.2	35.5		0.41
$Au/Fe(OH)_3$ CA	24.1		33.2	35.5	38.2[a]	0.85
$Au/Fe_2O_3^*$	24.1		33.2	35.5	38.2[a]	1.19
$Au/Fe(OH)_3^*${P}	24.1	30.2	33.2	35.5		0.47
α-Fe_2O_3 CA	24.1		33.2	35.5		1.27
γ-Fe_2O_3 CA		30.0		35.5		0
Fe_3O_4 CA		30.2		35.6		0

[a] Au(111) peak.

Raman spectra for $Au/Fe(OH)_3^*$(RT), $Au/Fe(OH)_3^*$ (473 K), $Au/Fe(OH)_3^*$, $Fe_2O_3^*$, and α-Fe_2O_3 CA in the 200–1600 cm^{-1} region are shown in Fig. 8. Raman bands for the reference compounds α-Fe_2O_3 CA, α-FeOOH CA, γ-FeOOH CA, γ-Fe_2O_3 CA, and Fe_3O_4 CA observed in this work are listed in Table 4. The positions of the characteristic Raman bands are generally in good agreement with those reported in the literature (24–28).

Six intense bands at 285, 400, 481, 600, 648, and 1298 cm^{-1} were observed in the Raman spectrum of specially prepared iron oxide $Fe_2O_3^*$ (Fig. 8d). Comparison with the reference compounds (Table 4) allowed us to ascribe all the bands except for 648 cm^{-1} to α-Fe_2O_3. The $Au/Fe(OH)_3^*$(RT) sample before calcination (Fig. 8a) revealed broad Raman bands of low intensity at 286, 402, 490, 602, 654, and 1317 cm^{-1}. Positions of the bands also corresponded to mainly α-Fe_2O_3. Under calcination at 473 and 673 K, general features of the Raman spectra and peak positions remained unchanged, but the intensities of the bands increased (Figs. 8b and

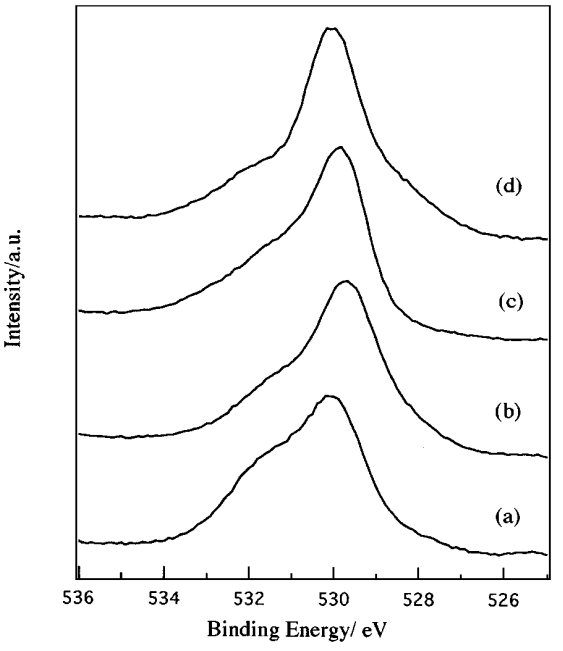

FIG. 7. XPS O 1s spectra of the $Au/Fe(OH)_3^*$ samples: (a) before calcination; (b) calcined at 473 K for 4 h; (c) calcined at 673 K for 4 h; and the support $Fe_2O_3^*$ (d).

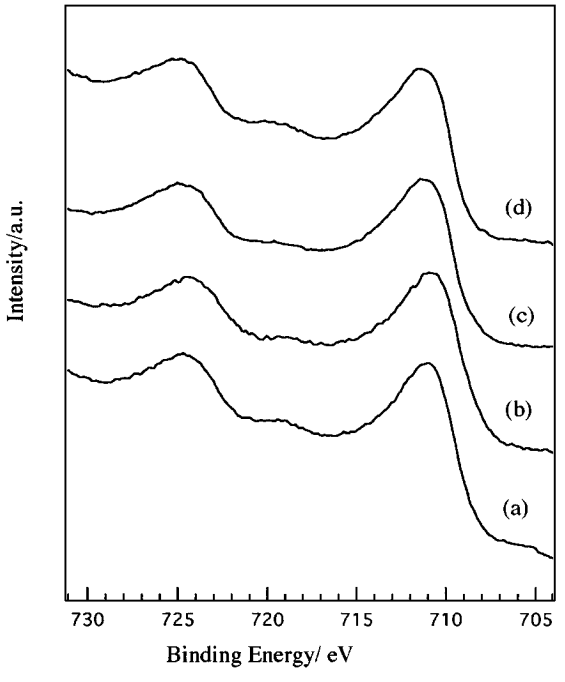

FIG. 6. XPS Fe 2p spectra of the $Au/Fe(OH)_3^*$ samples: (a) before calcination; (b) calcined at 473 K for 4 h; (c) calcined at 673 K for 4 h; and the support $Fe_2O_3^*$ (d).

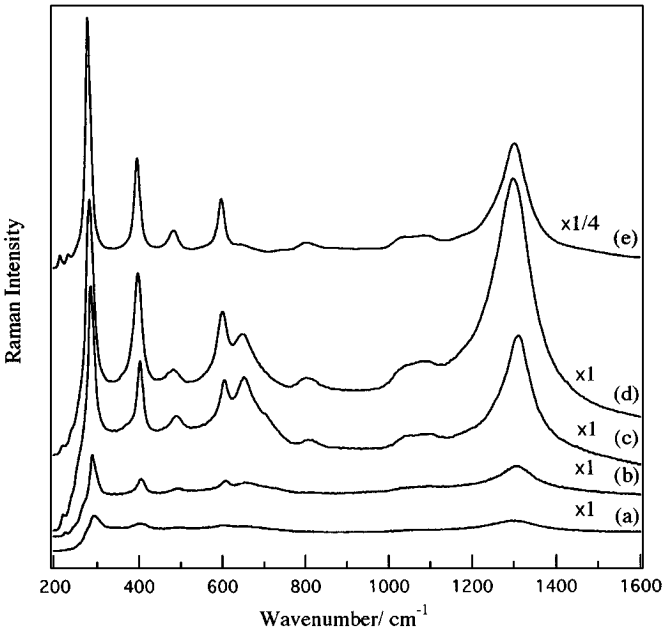

FIG. 8. Raman spectra of the $Au/Fe(OH)_3^*$ sample: (a) before calcination; (b) calcined at 473 K for 4 h; (c) calcined at 673 K for 4 h; the support $Fe_2O_3^*$ (d); and (e) reference α-Fe_2O_3 CA.

TABLE 4

Raman Bands (cm^{-1}) of Various Reference Iron Oxides and Oxyhydroxides

α-FeOOH	γ-FeOOH	α-Fe_2O_3	γ-Fe_2O_3	Fe_3O_4
vw 245	s 247	w 218	vw 285	
s 296	m 304	w 238	s 340	
ss 383	s 343	ss 285	sh 375	
sh 412	ss 374	s 402	s 501	w 530
m 478	s 522	m 487	s 630	
m 549	m 645	s 604	s 653	s 663
w 677	w 1293	w 807	s 714	
w 990		w 1000–1100	w 1420	
		s 1310		

Note. ss, very strong; s, strong; m, medium; w, weak; vw, very weak; sh, shoulder.

8c, respectively). The Raman spectrum of the Au/$Fe(OH)_3^*$ sample calcined at 673 K finally revealed the bands at 285, 405, 490, 607, 655, and 1313 cm^{-1} which positions coincide with those for $Fe_2O_3^*$ (Fig. 8c). In addition, a shoulder at $\sim$700 cm^{-1} was observed for the Au/$Fe(OH)_3^*$ samples after calcination at 473 and 673 K (Figs. 8b and 8c).

In-Situ IR Measurements

Results of *in-situ* FT-IR measurements for $Fe(OH)_3^*$-dried and Au/$Fe(OH)_3^*$ samples are shown in Figs. 9 and 10, respectively. The FT-IR spectra of the both samples before calcination exhibited broad and intensive absorbance at 2600–3650 cm^{-1}. The complexity of the band reflects the presence of a variety of OH groups in these starting materials and is mainly contributed by hydrogen-bonded hydroxyls and adsorbed water. In addition, three intensive bands in the 1300–1700 cm^{-1} region were observed for $Fe(OH)_3^*$-dried and Au/$Fe(OH)_3^*$(RT) samples. The band at about 1639 cm^{-1} can be attributed to H_2O bending. The

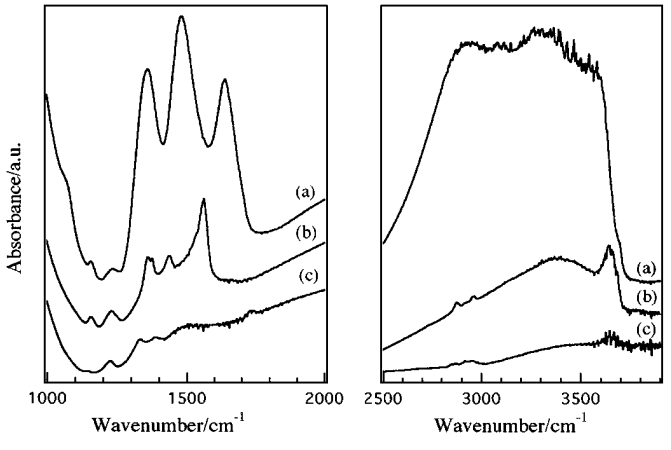

FIG. 9. *In-situ* FT-IR spectra of $Fe(OH)_3^*$-dried (a), $Fe(OH)_3^*$ (473 K) (b), and $Fe_2O_3^*$ (c).

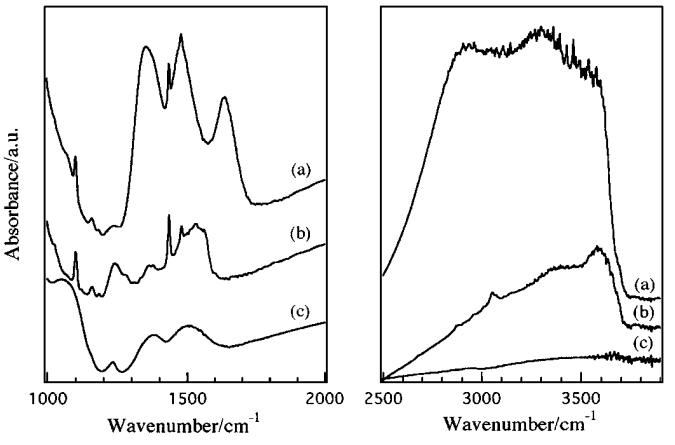

FIG. 10. *In-situ* FT-IR spectra of Au/$Fe(OH)_3^*$ (RT) (a), Au/$Fe(OH)_3^*$ (473 K) (b), and Au/$Fe(OH)_3^*$ (c).

other two broad and intensive bands centered at 1480 and 1360 cm^{-1} may be due to superposition of carbonate and nitrate species on the iron support (29, 30). Calcination up to 473 K resulted in the removal of physisorbed water because of the complete disappearance of the 1639 cm^{-1} band and significant decrease of absorbance in the 2600–3700 cm^{-1} region. Two bands at about 3640 and 3380 cm^{-1} can be distinguished for the $Fe(OH)_3^*$ (473 K) sample. The former peak can be ascribed to freely vibrating surface hydroxyl groups (31, 32). The peak shifted to 3585 cm^{-1} for the Au/$Fe(OH)_3^*$ (473 K) sample. Besides, a new band appeared at 3053 cm^{-1}. In the 1300–1700 cm^{-1} region after calcination up to 473 K a remarkable reduction in absorbance occurred. It corresponds to removal of the main portion of the surface nitrate and carbonate species. It is to be noted that at 473 K the $Fe(OH)_3^*$-dried sample showed the bands at 1230, 1361, 1376, 1436, and 1562 cm^{-1}, whereas the Au/$Fe(OH)_3^*$ (473 K) sample exhibited bands at 1240 and 1368 and a broad complex band centered at about 1535 cm^{-1}. The difference in their relative intensities and in peak positions can be explained by a different population of surface carbonates with various conformations and nitrates adsorbed on the supports. The relatively sharp IR bands at 1099, 1438, and 1493 cm^{-1} in Fig. 10b are due to gold precursor Au(PPh_3)(NO_3) which was still present in the Au/$Fe(OH)_3^*$ (473 K) sample. These bands disappeared by calcination up to 673 K (Fig. 10c). The $Fe(OH)_3^*$-dried sample exhibited no strong absorbance band in the 1000–4000 cm^{-1} region after calcination at 673 K, while the Au/$Fe(OH)_3^*$ sample calcined at 673 K showed broad signals at 1060, 1380, and 1510 cm^{-1}. The former of them can be assigned to surface phosphate species (33).

DISCUSSION

Activities of iron oxide supported gold catalysts in CO oxidation vary from excellent performance of Au/$Fe(OH)_3^*$

and $Au/Fe(OH)_3^*$-dried samples to no catalytic performance of $Au/Fe(OH)_3$ CA and Au/α-Fe_2O_3 CA until 400–500 K (Figs. 1 and 2). Under the reaction conditions applied, the steady-state rates of CO oxidation for $Au/Fe(OH)_3^*$ and $Au/Fe(OH)_3^*$-dried catalysts were 0.0064 at 203 K and 0.0039 at 208 K [mol CO (mol-Au)$^{-1}$ s^{-1}], respectively (Table 1). Accurate comparison with the reported data cannot be done due to the differences in Au-loadings and reaction conditions applied, but the Au/Fe_2O_3-coprecipitated sample prepared according to the literature (5, 6) showed reaction rate as low as 0.0002 mol CO (mol-Au)$^{-1}$ s^{-1} at 234 K.

We have demonstrated clearly that tremendous catalysis of Au can be achieved when as-precipitated wet iron hydroxide $Fe(OH)_3^*$ is used as a support for $Au(PPh_3)(NO_3)$. The type of support applied may influence the catalytic activity through control of the Au particle size or through formation of highly active sites on the Au particle–iron oxide interface. Previous researchers suggested that small gold particles and the interface are responsible for high activity of metal oxide supported gold catalysts (16, 34). The highly dispersed state of Au in supported Au catalysts is believed to be formed as a result of specific interaction of a gold precursor with a support. The strength of metal–support interactions is generally controlled by the macroscopic properties of the support surface such as morphology, crystallinity, surface area, chemical composition, OH groups, and defects. To understand the origin of the high activity of the $Fe(OH)_3^*$-supported Au catalysts, comparative characterization of both various starting supports and final Au-containing catalytic materials has been performed by different bulk and surface physical techniques.

It is known that among macroscopic factors, morphology and specific surface area of catalyst supports have an influence on the performance of heterogeneous catalysts. Indeed, the increase of CO oxidation activity in the series of commercially available supports Au/α-Fe_2O_3 CA (5 m^2 g^{-1}) < $Au/Fe(OH)_3$ CA (47 m^2 g^{-1}) < Au/α-FeOOH CA (84 m^2 g^{-1}) indicates that BET surface area (S_{BET}) is an important factor for the CA support-derived catalysts. On the other hand, the samples with a high level of catalytic activity such as $Au/Fe(OH)_3^*$ (63 m^2 g^{-1}), $Au/Fe(OH)_3^*$-dried (57 m^2 g^{-1}), and $Au/Fe(OH)_3^*${P} (60 m^2 g^{-1}) possessed S_{BET} values that were comparable to 55 m^2 g^{-1} of the low-active $Au/Fe_2O_3^*$ sample (Table 2). SEM images (Fig. 3) and S_{BET} (Table 2) of the gold-containing sample $Au/Fe(OH)_3^*$ and PPh_3-treated support $Fe(OH)_3^*${P} are similar to each other. The triphenylphosphine ligand obviously affects morphology of the final catalyst through support modification and surface reconstruction. The catalytic performances of $Au/Fe(OH)_3^*$ and $Fe(OH)_3^*${P} differ essentially, but supporting $Au(PPh_3)(NO_3)$ on the PPh_3-treated support $Fe(OH)_3^*${P} allowed us to obtain a catalyst with markedly improved activity in comparison with the application of non-PPh_3-treated support $Fe_2O_3^*$ (Fig. 2). Thus, the high catalytic activity of the $Fe(OH)_3^*$-supported samples cannot be fully explained by the differences in the specific surface area and morphology of the catalyst support, and therefore microscopic investigations on the state and composition of both starting supports and final catalytic materials are necessary.

It is to be noted that supporting the gold complex to commercially available wet $Fe(OH)_3$ did not result in the sample with a high catalytic activity. If the property of the commercially available $Fe(OH)_3$ CA is similar to that of the as-precipitated iron hydroxide $Fe(OH)_3^*$, one could expect the same level of activity for the resultant supported Au catalysts. Significant difference of $Fe(OH)_3^*$ from $Fe(OH)_3$ CA was revealed from XRD measurements (Fig. 4). The as-precipitated $Fe(OH)_3^*$ exhibited no XRD peak between 20 and 70° 2Θ, while the other supports employed in this work, including $Fe(OH)_3$ CA, are crystalline solids. The amorphous state of $Fe(OH)_3^*$ was also confirmed by TGA; weight loss took place gradually, without any clear transformation point until 673 K. Such a kind of material should contain a large amount of bound water in the form of OH groups, as their amount increases with increasing amount of amorphous part of an oxide (35). It was found by Andreeva *et al.* for Au/α-Fe_2O_3-coprecipitated samples that changing the pH value gradually during a coprecipitation step resulted in amorphous precipitates, while the deposition process at constant pH value led to a definite α-FeOOH phase (10). Total weight loss for the $Fe(OH)_3^*$-dried sample under heating up to 773 K was estimated to be 20.9%, while for crystalline α-FeOOH the total weight loss is reported to be 13.8% in the same temperature range (36). Comparison of the values of total weight losses indicates that the samples possess different degrees of hydration; i.e., even after drying the amorphous $Fe(OH)_3^*$ in a vacuum it contains a larger amount of water, as compared to the crystalline support α-FeOOH. Thus, the degree of support hydration is associated with support crystallinity. Moreover, the amorphous material may contain many surface defects that should also increase Au-support interactions and therefore prevent gold from agglomerating into larger Au particles.

Analysis of the XRD data of $Au/Fe(OH)_3^*$, $Fe(OH)_3^*${P}, and $Au/Fe(OH)_3^*${P} samples calcined at 673 K (Figs. 4 and 5) revealed their low crystallinity and the appearance of the additional XRD peak at the 2Θ value of 30°. The peak position does not belong to the one characteristic of hematite α-Fe_2O_3, but it can be ascribed to either γ-Fe_2O_3 or Fe_3O_4. We suggest that probably the Au precursor retarded the iron oxide crystallization process and promoted the formation of γ-Fe_2O_3. Supported gold catalysts obtained by a coprecipitation method have been subject of much research to date. It was suggested that the presence of gold in the coprecipitated mixtures of Au/Fe, Au/Ni, and Au/Co

may influence morphology and textural properties of the metal oxide supports (5). The fact that the catalytic materials possessed larger specific surface areas than that of the pure oxides is supposed to be due to retarding the support crystal growth by gold. It was also reported by Hutchings *et al.* (13) that for Au/CuO and Au/ZnO coprecipitated catalysts the presence of Au in the precipitated mixtures suppressed the crystallization process of the supports, and the final materials after aging for 300 min were nearly amorphous, although the absence of Au in the same mixtures led to crystallized supports even after a much shorter aging time. It is known that the addition of small amounts of impurity metal cations can influence crystallization processes (33, 37, 38). In particular, the presence of Co and Cu additives is known to inhibit the formation of the α-Fe_2O_3 phase (35, 38). Formation of the γ-Fe_2O_3 phase in the iron oxide systems was observed to be promoted by the presence of small amounts of metal cations such as Co (37, 39). The low crystallinity of the iron oxide support in the Au/$Fe(OH)_3^*$ sample, as well as the γ-Fe_2O_3 formation, in comparison with the iron oxide support in the Au/$Fe_2O_3^*$, may be explained by assuming similar properties of gold. It should be noted, however, that no other iron oxide phase except for α-Fe_2O_3 has been reported for the Au/Fe_2O_3 samples prepared by a coprecipitation method (4, 5, 9, 10). Close similarity of the SEM images and XRD patterns of the gold-containing sample Au/$Fe(OH)_3^*$ and the PPh_3-treated support $Fe(OH)_3^*${P} allowed us to suggest that the presence of triphenylphosphine ligand is the most important factor that influenced the morphology and surface structure of the iron oxide support. Since crystallization of the amorphous support $Fe(OH)_3^*$ proceeded in the presence of the phosphine, it is reasonable to suggest the reduction of a part of Fe^{3+} to Fe^{2+} by the PPh_3 and the formation of the mixed-valence iron oxide Fe_3O_4 as shown in Scheme 1. As the samples underwent the heating treatment under oxidative conditions, the Fe_3O_4 formed can be oxidized to produce γ-Fe_2O_3. The oxidation can proceed at moderate temperatures (393–483 K), depending on Fe_3O_4 particle size, while further transformation of the γ-Fe_2O_3 into α-Fe_2O_3 demands much higher temperatures (773– 873 K) (40). The shift of the XPS Fe $2p_{3/2}$ peak

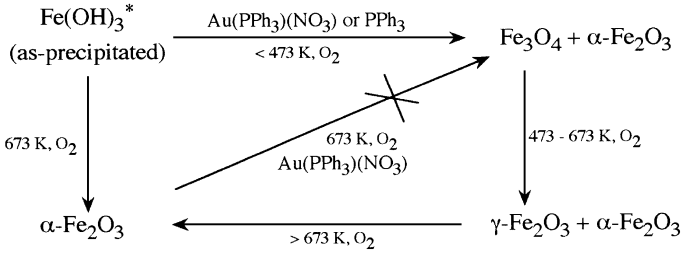

SCHEME 1. Transformations of the as-precipitated $Fe(OH)_3^*$ in the presence and absence of $Au(PPh_3)(NO_3)$ or PPh_3.

for Au/$Fe(OH)_3^*$ (473 K) sample to 710.8 eV could be an indication of the formation of mixed-valence oxide Fe_3O_4 according to the literature (22, 23, 41, 42). However, the small difference in the O 1s binding energies of Fe_2O_3 and Fe_3O_4 makes it difficult to argue detection of Fe_3O_4 phase by XPS for the Au/$Fe(OH)_3^*$ (473 K) sample.

Laser Raman spectroscopy allows us to characterize the samples composed of iron oxides with the same chemical composition but different crystal structures. The data for various reference compounds listed in Table 4 agree well with the literature (24–28) and confirm that the iron oxides and oxyhydroxides can be distinguished by their specific Raman bands. There was no evidence for the existence of oxyhydroxides α- and γ-FeOOH on the surface of the Au/$Fe(OH)_3^*$ catalyst at any stage of the preparation; α-FeOOH is characterized by the distinctive bands at 383 and 296 cm^{-1}, and γ-FeOOH is characterized by the bands at 343 and 247 cm^{-1}, and no other iron oxides have intense bands at these positions (Table 4). The Raman spectra of Au/$Fe(OH)_3^*$ and $Fe_2O_3^*$ after calcination at 673 K (Figs. 8c and 8d) possessed six intense bands in the region 200–1600 cm^{-1}. Five of them coincided with bands at 285, 402, 487, 604, and 1310 cm^{-1} for reference α-Fe_2O_3 (Table 4, Fig. 8e). The Raman spectra in Figs. 8c–8e showed the weak bands at ~800 and the broad bands at 1000–1100 cm^{-1}. The similarity of these spectra in peak positions and intensity ratios also supports the assignment. Interestingly, the Au/$Fe(OH)_3^*$(RT) sample before calcination (Fig. 8a) revealed weak and broad Raman bands at the same positions as those for $Fe_2O_3^*$ and Au/$Fe(OH)_3^*$, indicating the presence of α-Fe_2O_3 crystallites on the surface, although no XRD peaks were observed with the Au/$Fe(OH)_3^*$(RT) sample. As for the Au/Fe_2O_3 sample prepared by a coprecipitation method, the presence of ferrihydrite, α-Fe_2O_3 and α-FeOOH in the sample before calcination was suggested by Mössbauer spectroscopy (43). As the crystallinity of the support in Au/$Fe(OH)_3^*$ increased by calcination, the intensities of the Raman spectra increased from Figs. 8a to 8c. The additional Raman feature appeared at 655 cm^{-1} for Au/$Fe(OH)_3^*$ and can be ascribed to γ-Fe_2O_3 rather than Fe_3O_4 in accordance to the reference data in Table 4. However, the presence of the Raman band at similar position (648 cm^{-1}) for the $Fe_2O_3^*$ makes the assignment doubtful. While the band is absent in the spectra of single-crystal α-Fe_2O_3, it is observed for polycrystalline α-Fe_2O_3 films concomitantly with the six Raman-allowed phonons at 218 (A_{1g}), 238 (E_g), 285 ($2E_g$), 402 (A_{1g}), 487 (E_g), 604 (E_g) cm^{-1}, and the band at 1310 cm^{-1}. The band near 650 cm^{-1} was ascribed to be due to a Raman-forbidden longitudinal optical (LO) phonon caused by defect-induced scattering (44). While the Raman-allowed 2LO line near 1300 cm^{-1} (at roughly twice LO frequency) is usually seen in the spectra for any α-Fe_2O_3, a large amount of defects in polycrystalline films make the LO line observable also

(45). As for the shoulder at about 700 cm^{-1} in the Raman spectra of $Au/Fe(OH)_3^*$ calcined at 473 and 673 K, its appearance can be ascribed to γ-Fe_2O_3 rather than Fe_3O_4. In addition, our measurements revealed that α-Fe_2O_3 was a much stronger scatterer, as compared to γ-Fe_2O_3 and Fe_3O_4, similarly to the previous observations for α-Fe_2O_3 (24, 25). Thibeau *et al.* showed that in a physical mixture of α-Fe_2O_3 and Fe_3O_4, 5% α-Fe_2O_3 was enough for its identification, but more than 30% Fe_3O_4 was required for its detection in the mixture (24). As we performed no special calibration, our data can provide qualitative information about the surface composition of $Au/Fe(OH)_3^*$ due to different sensitivity towards various iron oxide polymorphs. Nevertheless, the presence of γ-Fe_2O_3 on the support surface in $Au/Fe(OH)_3^*$ can be concluded in agreement with the XRD data. Possibly, the γ-Fe_2O_3 formation may be considered as an indication of the occurrence of stronger interactions between $Au(PPh_3)(NO_3)$ and $Fe(OH)_3^*$. The results of the catalytic tests for the various α- and γ-Fe_2O_3-containing samples (Fig. 2) allowed us to suggest that the γ-phase is an important component of the catalytic Au-containing materials.

Defects and OH groups of support surfaces can significantly modify the interaction between metal-complex precursor and oxide support and, hence, catalytic activity of the resultant supported metals (46). The XPS O 1s spectrum of the $Au/Fe(OH)_3^*$ sample revealed a larger shoulder at about 532 eV, in comparison with that of $Fe_2O_3^*$ (Fig. 7). The higher BE peak can be ascribed to OH-groups at the support surface. However, care should be taken in the interpretation of the XPS O 1s data. As will be described elsewhere (47), phosphorus oxygen species remain in $Au/Fe(OH)_3^*$ during the course of calcination and contribution of the species to the XPS O 1s peak around 532 eV does not allow us to make clear conclusions about the amount of OH groups from the XPS data. More reliable information about physisorbed water and surface OH groups was obtained from *in situ* FT-IR spectra (Figs. 9 and 10). The $Fe(OH)_3^*$ and $Au/Fe(OH)_3^*$ samples before calcination showed intensive peaks at 1639 cm^{-1} and in the region 2600–3700 cm^{-1} due to presence of large amounts of OH groups and absorbed water. Probably, they promoted interactions between the gold and support precursors. An indirect argument for occurrence of such interactions can be obtained from the FT-IR spectra of the materials calcined up to 473 K. The ν_{OH} peak at 3640 cm^{-1} in the $Fe(OH)_3^*$ (473 K) sample (Fig. 9b) shifted to 3585 cm^{-1} by 55 cm^{-1} by supporting the Au complex ($Au/Fe(OH)_3^*$ (473 K)) (Fig. 10b), which assumes occurrence of an interaction between the surface OH groups and the Au precursor. The interaction should reduce the mobility of Au species on the iron oxide support and hence result in the formation of small Au particles in the final catalytic material $Au/Fe(OH)_3^*$. Mobility of Au species on the oxide surface can also be sufficiently lowered by the presence of a lot of defects (48). Laser Raman spectra in Fig. 8 indicated large amounts of the support defects in the active $Au/Fe(OH)_3^*$ catalyst as discussed above. Formation of about 10 times larger Au particles when Fe_2O_3 was used as support, instead of $Fe(OH)_3^*$ (30 and 2.9 nm, respectively) (18) coincides with the suggestion about the occurrence of stronger interactions between the $Au(PPh_3)(NO_3)$ and OH-groups and defects of the amorphous iron hydroxide.

CONCLUSIONS

(1) It was found that the $Au/Fe(OH)_3^*$ catalyst was superior to the other catalysts in low-temperature CO oxidation.

(2) Starting iron-oxide supports and resulting supported Au catalysts were characterized and compared by various surface and bulk techniques. The characterization revealed that the initial state and structure of the supports are very important for preparation of active Au catalysts.

(3) Crystallization of the iron oxide support in the presence of the phosphine-ligated gold complex resulted in poorly crystallized iron oxide support consisting of a mixture of α-Fe_2O_3 and γ-Fe_2O_3.

(4) The most probable mechanism of the γ-Fe_2O_3 formation includes reduction of a part of Fe^{3+} to Fe^{2+} by the PPh_3 ligand to produce mixed-valence iron oxide Fe_3O_4, followed by reoxidation of the magnetite to γ-Fe_2O_3. The suggested transformation scheme was supported by XRD and laser Raman data.

(5) No γ-Fe_2O_3 formation was observed when $Au(PPh_3)(NO_3)$ was decomposed on the other supports. γ-Fe_2O_3 seems to be an important phase to promote the catalytic activity of iron oxide supported Au catalysts for the low-temperature CO oxidation.

(6) Application of the amorphous $Fe(OH)_3^*$ may prevent Au species from aggregation through stabilization of $Au(PPh_3)(NO_3)$ by interactions with OH-groups and defects of the support, leading to formation of small gold metallic particles.

ACKNOWLEDGMENTS

The authors thank Professor H. Shindo, Chuo University for helping us in measuring Raman spectra. This work has been supported by Core Research for Evolutional Science and Technology (CREST) of Japan Science and Technology Corporation (JST).

REFERENCES

1. Ponec, V., and Bond, G. C., "Catalysis by Metals and Alloys," *Stud. Surf. Sci. Catal.*, Vol. 95. Elsevier, Amsterdam, 1995.
2. Bond, G. C., *Chem. Soc. Rev.* **20**, 441 (1991).
3. Huber, H., McIntosh, D., and Ozin, G. A., *Inorg. Chem.* **16**, 975 (1977).
4. Haruta, M., Kobayashi, T., Sano, H., and Yamada, N., *Chem. Lett.*, 405 (1987).
5. Haruta, M., Yamada, N., Kobayashi, T., and Iijima, S., *J. Catal.* **115**, 301 (1989).

6. Haruta, M., Tsubota, S., Kobayashi, T., Kageyama, H., Genet, M. J., and Delmon, B., *J. Catal.* **144**, 175 (1993).
7. Haruta, M., Ueda, A., Tsubota, S., and Torres-Sanchez, R. M., *Catal. Today* **29**, 443 (1996).
8. Sakurai, H., and Haruta, M., *Appl. Catal. A: General* **127**, 93 (1995).
9. Andreeva, D., Idakiev, V., Tabakova, T., and Andreev, A., *J. Catal.* **158**, 354 (1996).
10. Andreeva, D., Idakiev, V., Tabakova, T., Andreev, A., and Giovanoli, R., *Appl. Catal. A: General* **134**, 275 (1996).
11. Ueda, A., Kobayashi, T., and Haruta, M., *Shokubai (Catal. & Catal.)* **39**, 125 (1997).
12. Gardner, S. D., Hoflund, G. B., Schryer, D. R., Schryer, J., Upchurch, B. T., and Kielin, E. J., *Langmuir* **7**, 2135 (1991).
13. Hutchings, G. J., Siddiqui, M. R. H., Burrows, A., Kiely, C. J., and Whyman, R., *J. Chem. Soc. Faraday Trans.* **93**, 187 (1997).
14. Hoflund, G. B., Gardner, S. D., Schryer, D. R., Upchurch, B. T., and Kielin, E. J., *Appl. Catal. B: Environ.* **6**, 117 (1995).
15. Baiker, A., Maciejewski, M., Tagliaferri, S., and Hug, P., *J. Catal.* **151**, 407 (1995).
16. Haruta, M., *Catal. Surveys of Japan* **1**, 61 (1997).
17. Yuan, Y., Asakura, K., Wan, H., Tsai, K., and Iwasawa, Y., *Chem. Lett.*, 755 (1996).
18. Yuan, Y., Kozlova, A. P., Asakura, K., Wan, H., Tsai, K., and Iwasawa, Y., *J. Catal.* **170**, 191 (1997).
19. Schwarz, J. A., Contescu, C., and Contescu, A., *Chem. Rev.* **95**, 477 (1995).
20. Mueting, A. M., Alexander, B. D., Boyle, P. D., Casalnuovo, A. L., Ito, L. N., Johnson, B. J., and Pignolet, L. H., *in* "Inorganic Syntheses" (R. N. Grimes, Ed.), Vol. 29, p. 280. Wiley, New York, 1992.
21. Wagner, C. D., Riggs, W. M., Davis, L. E., Moulder, J. F., and Mullenberg, G. E. (Eds.), "Handbook of X-ray Photoelectron Spectroscopy: A Reference Book of Standard Data for Use in X-ray Photoelectron Spectroscopy." Perkin-Elmer, Minnesota, 1979.
22. Kuivila, C. S., Butt, J. B., and Stair, P. C., *Appl. Surf. Sci.* **32**, 99 (1988).
23. Brundle, C. R., Chuang, T. J., and Wandelt, K., *Surf. Sci.* **68**, 459 (1977).
24. Thibeau, R. J., Brown, C. W., and Heiderbach, R. H., *Appl. Spectrosc.* **32**, 532 (1978).
25. Ohtsuka, T., Kubo, K., and Sato, N., *Corrosion (Houston)* **42**, 476 (1986).
26. Johnston, C., *Vib. Spectrosc.* **1**, 87 (1990).
27. Gui, J., and Devine, T. M., *Corros. Sci.* **32**, 1105 (1991).
28. Nauer, G., Strecha, P., Brinda-Konopik, N., and Liptay, G., *J. Therm. Anal.* **30**, 813 (1985).
29. Lee, J. S., Kim, S., and Kim, Y. G., *Top. Catal.* **2**, 127 (1995).
30. Guglielminotti, E., and Boccuzzi, F., *Appl. Catal. B: Environ.* **8**, 375 (1996).
31. Lorenzelli, V., Rossi, P. F., Busca, G., and Cotena, N., *in* "Heterog. Catal., Proc. Int. Symp., 4th, Pt. 1, 1979," p. 463.
32. Tsyganenko, A. A., and Filimonov, V. N., *Spectrosc. Lett.* **5**, 477 (1972).
33. Dolphin, D., and Wick, A., "Tabulation of Infrared Spectral Data." Wiley, New York, 1977.
34. Haruta, M., *Catal. Today* **36**, 153 (1997).
35. Furuichi, R., Sato, N., and Okamoto, G., *Chimia* **23**, 455 (1969).
36. Tabakova, T., Andreeva, D., Idakiev, V., Andreev, A., and Giovanoli, R., *J. Mater. Sci.* **31**, 1101 (1996).
37. Shopov, D., and Andreev, A., *Kinet. Catal. (Engl. Transl.)* **28**, 133 (1987).
38. Cornell, R. M., and Giovanoli, R., *Polyhedron* **7**, 385 (1988).
39. Neshev, N., Idakiev, V., Halachev, T., Andreeva, D., Marinova, T. Z., and Andreev, A., *Commun. Dep. Chem.* **22**, 94 (1989).
40. von Egger, K., and Feitknecht, W., *Helv. Chim. Acta* **45**, 2042 (1962).
41. Epling, W. S., Hoflund, G. B., Weaver, J. F., Tsubota, S., and Haruta, M., *J. Phys. Chem.* **100**, 9929 (1996).
42. Sault, A. G., *Appl. Surf. Sci.* **74**, 249 (1994).
43. Wagner, F. E., Galvagno, S., Milone, C., Visco, A. M., Stievano, L., and Calogero, S., *J. Chem. Soc. Faraday Trans.* **93**, 3403 (1997).
44. Massey, M. J., Baier, U., Merlin, R., and Waber, W. H., *Phys. Rev. B* **41**, 7822 (1990).
45. McCarty, K. F., *Solid State Commum.* **68**, 799 (1988).
46. Iwasawa, Y., Ed., "Tailored Metal Catalysts." Reidel, Dordrecht, 1986.
47. Kozlova, A. P., Kozlov, A. I., Asakura, K., and Iwasawa, Y., to be published.
48. Kubo, M., Stirling, A., Miura, R., Yamauchi, R., and Miyamoto, A., *Catal. Today* **36**, 143 (1997).